JGR Atmospheres

RESEARCH ARTICLE
10.1029/2019JD031662

Secondary Gravity Waves Generated by Breaking Mountain Waves Over Europe

C. J. Heale[1], K. Bossert[2], S. L. Vadas[3], L. Hoffmann[4], A. Dörnbrack[5], G. Stober[6], J. B. Snively[1], and C. Jacobi[7]

[1]Center for Space and Atmospheric Research (CSAR), Embry-Riddle Aeronautical University, Daytona Beach, FL, USA, [2]Department of Electrical & Computer Engineering, University of Alaska, Fairbanks, AK, USA, [3]NorthWest Research Associates, Inc., Boulder, CO, USA, [4]Jülich Supercomputing Centre, Forschungszentrum Jülich, Jülich, Germany, [5]DLR, Institut für Physik der Atmosphäre, Oberpfaffenhofen, Germany, [6]Institute of Applied Physics, University of Bern, Bern, Switzerland, [7]Institute for Meteorology, University of Leipzig, Leipzig, Germany

Key Points:
- Mountain wave breaking in the MLT couples directly to secondary waves
- Tidal winds act like a filter for secondary wave spectra reaching the thermosphere
- Nonprimary wave forcing is significant and distribution is governed by thermospheric winds

Supporting Information:
- Supporting Information S1
- Movie S1
- Movie S2

Correspondence to:
C. Heale,
healec@erau.edu

Citation:
Heale, C. J., Bossert, K., Vadas, S. L., Hoffmann, L., Dörnbrack, A., Stober, G., et al. (2020). Secondary gravity waves generated by breaking mountain waves over Europe. *Journal of Geophysical Research: Atmospheres*, *125*, e2019JD031662. https://doi.org/10.1029/2019JD031662

Received 13 SEP 2019
Accepted 18 FEB 2020
Accepted article online 19 FEB 2020

Abstract A strong mountain wave, observed over Central Europe on 12 January 2016, is simulated in 2D under two fixed background wind conditions representing opposite tidal phases. The aim of the simulation is to investigate the breaking of the mountain wave and subsequent generation of nonprimary waves in the upper atmosphere. The model results show that the mountain wave first breaks as it approaches a mesospheric critical level creating turbulence on horizontal scales of 8–30 km. These turbulence scales couple directly to horizontal secondary waves scales, but those scales are prevented from reaching the thermosphere by the tidal winds, which act like a filter. Initial secondary waves that can reach the thermosphere range from 60 to 120 km in horizontal scale and are influenced by the scales of the horizontal and vertical forcing associated with wave breaking at mountain wave zonal phase width, and horizontal wavelength scales. Large-scale nonprimary waves dominate over the whole duration of the simulation with horizontal scales of 107–300 km and periods of 11–22 minutes. The thermosphere winds heavily influence the time-averaged spatial distribution of wave forcing in the thermosphere, which peaks at 150 km altitude and occurs both westward and eastward of the source in the 2 UT background simulation and primarily eastward of the source in the 7 UT background simulation. The forcing amplitude is ~2× that of the primary mountain wave breaking and dissipation. This suggests that nonprimary waves play a significant role in gravity waves dynamics and improved understanding of the thermospheric winds is crucial to understanding their forcing distribution.

1. Introduction

Gravity waves (GWs) play an important role in the transport of energy and momentum from the lower to the middle and upper atmosphere (e.g., Fritts & Alexander, 2003; Garcia & Solomon, 1985; Holton, 1982; Lindzen, 1981; Vadas et al., 2014; Yiğit & Medvedev, 2015). Through dissipation mechanisms such as viscosity, critical level filtering, and wave breaking, waves can deposit their energy and momentum into the mean state causing localized forcing of the mean winds and heating/cooling of the atmosphere (Fritts & Alexander, 2003; Heale et al., 2018, 2014; Hickey et al., 2011; Holton, 1983; Holton & Alexander, 2000; Lund & Fritts, 2012; McFarlane, 1987; Vadas, 2007; Vadas et al., 2003; Vadas & Fritts, 2005). The influence of gravity wave forcing contributes to atmospheric phenomena such as the quasi-biennial oscillation (QBO) (Alexander & Holton, 1997; Baldwin et al., 2001; Dunkerton, 1997; Ern et al., 2014; Piani et al., 2000), the summer branch of the Brewer-Dobson circulation (Alexander & Rosenlof, 2003; Stephan et al., 2016), and the cold summer mesopause (Alexander & Rosenlof, 1996; Garcia & Solomon, 1985; Holton & Alexander, 2000).

One important source of gravity wave generation is via flow over topography (also known as orographic or mountain waves) (Bacmeister, 1993; Dörnbrack et al., 1999; Durran & Klemp, 1987; McFarlane, 1987; McLandress et al., 2012; Nastrom & Fritts, 1992; Smith, 1979). The lifting of surface level winds as it flows over the terrain leads to the generation of quasi-stationary waves (approximately zero relative ground period) that propagate upwards into the atmosphere (Nappo, 2002). Hotspots for such waves exist over mountainous regions of the world such as the South American Andes, the European alps and Scandinavian mountains,

New Zealand, and Antarctica (Hoffmann et al., 2013) where the flow near the mountain tops are approximately perpendicular to the mountain range. A unique feature of these mountain waves is that they can only exist in the presence of a mean background wind. If the mountain wave encounters a region of zero wind, the layer acts as a critical level and filters the wave into the mean flow (Booker & Bretherton, 1967). In the summertime, winds switch between eastward and westward directions in the middle atmosphere; thus, mountain waves tend to get filtered in the stratosphere. However, in the wintertime, the winds do not typically reverse sign until the mesosphere, and thus, mountain waves can propagate up to these altitudes and obtain larger amplitudes before being filtered. As such, mountain waves tend to dominate in the wintertime (Hoffmann et al., 2013). As the mountain wave approaches the critical level, it is refracted to smaller vertical scale. The smaller vertical scale, at large amplitudes, lead to large vertical gradients in the wind and temperature structure of the wave, which can cause the mountain wave to break. The wave breaking creates turbulence and generates secondary acoustic-gravity waves (Bacmeister & Schoeberl, 1989; Bossert et al., 2017; Ehard et al., 2016; Heale et al., 2017; Satomura & Sato, 1999; Smith et al., 2013; Vadas et al., 2018).

Secondary gravity waves are categorized by two mechanisms: linear and nonlinear generation (furthermore referred to as nonprimary waves since the dissipation and new wave generation process can happen multiple times). The linear mechanism arises as a primary wave dissipates as a whole. The dissipation exerts a body force on the mean flow at packet scale, which generates a spectra of nonprimary waves with larger scales and longer periods than the primary wave. The theory for these waves is described in Vadas et al. (2003, 2018) and such waves have been identified over Antarctica via identifying characteristic fishbone patterns in lidar data and simulation results. In contrast, the nonlinear mechanism is associated wave breaking and the cascade to smaller scales (e.g., Achatz, 2007; Andreassen et al., 1994; Bacmeister & Schoeberl, 1989; Dörnbrack, 1998; Franke & Robinson, 1999; Fritts et al., 2009; Horinouchi et al., 2002; Lund & Fritts, 2012; Satomura & Sato, 1999; Snively & Pasko, 2003). The theory being that breaking produces localized forcing at the turbulent scales and periods, which generate nonprimary gravity waves (Chun & Kim, 2008; Kim & Chun, 2008; Song et al., 2003; Zhou et al., 2002). As such, these nonprimary waves are expected to have scales and periods that are smaller than those of the primary breaking wave. There is debate, however, over the dominance and importance of each mechanism.

The DEEPWAVE campaign (e.g., Fritts et al., 2016) used coordinated observations and modeling to study the propagation of mountain waves over New Zealand from the ground to the thermosphere (e.g., Bramberger et al., 2017; Bossert et al., 2015; Eckermann et al., 2016; Kaifler et al., 2017; Smith et al., 2016). The campaign found that there was often a multiscale wave environment in the mesosphere within the phases of a larger scale mountain wave (Bossert et al., 2015). Further studies suggested that the mountain wave would break in the mesosphere, generating quasi-stationary eddy structures and propagating nonprimary waves. Observation techniques, such as airglow imaging, make it difficult to identify the difference between the turbulent and nonprimary wave structures because it measures integrated values over a layer. However, turbulent and wave structures were identified in height-dependent lidar data (Bossert et al., 2017; Heale et al., 2017). The campaign revealed that mesospheric activity and wave breaking was present on days where surface wind forcing was small. If the surface wind forcing was too large, the mountain wave would break in the stratosphere, due to having a large amplitude, and would dissipate before reaching the mesosphere (Ehard et al., 2017; Fritts et al., 2018; Kaifler et al., 2015). Despite significant advancement, very little is still known about the spectra and importance of nonprimary waves in the upper atmosphere. Most general circulation models (GCMs) are hydrostatic and only resolve inertia gravity waves that have long periods and act in an incompressible manner. Smaller wavelength, shorter period acoustic gravity waves (AGWs), which can require compressible effects, have to be parameterized in these models (Kim et al., 2003). Nonprimary waves can repopulate parts of the phase speed spectrum that have encountered a critical level below. Thus, we could miss important physics that cannot be described by tropospheric sources. Therefore, their study remains an important topic in advancing our understanding of the effects of GWs on the atmosphere as a whole.

In this paper, we use the time-dependent, fully nonlinear, high-resolution numerical model, known as MAGIC (Model for Acoustic and Gravity wave Interactions in a Compressible atmosphere) (Snively, 2013; Snively & Pasko, 2008; Zettergren & Snively, 2015) to simulate a mountain wave from the ground to 300-km altitude, in 2D. The simulation is based upon a mountain wave observed over Central Europe on 12 January 2016. In particular, we focus on the nonlinearity, wave breaking, and nonprimary wave generation of the mountain wave in the mesosphere and thermosphere regions of the atmosphere assuming two different solar tidal phases. We aim to elucidate the coupling mechanisms and spectra of nonprimary waves generated

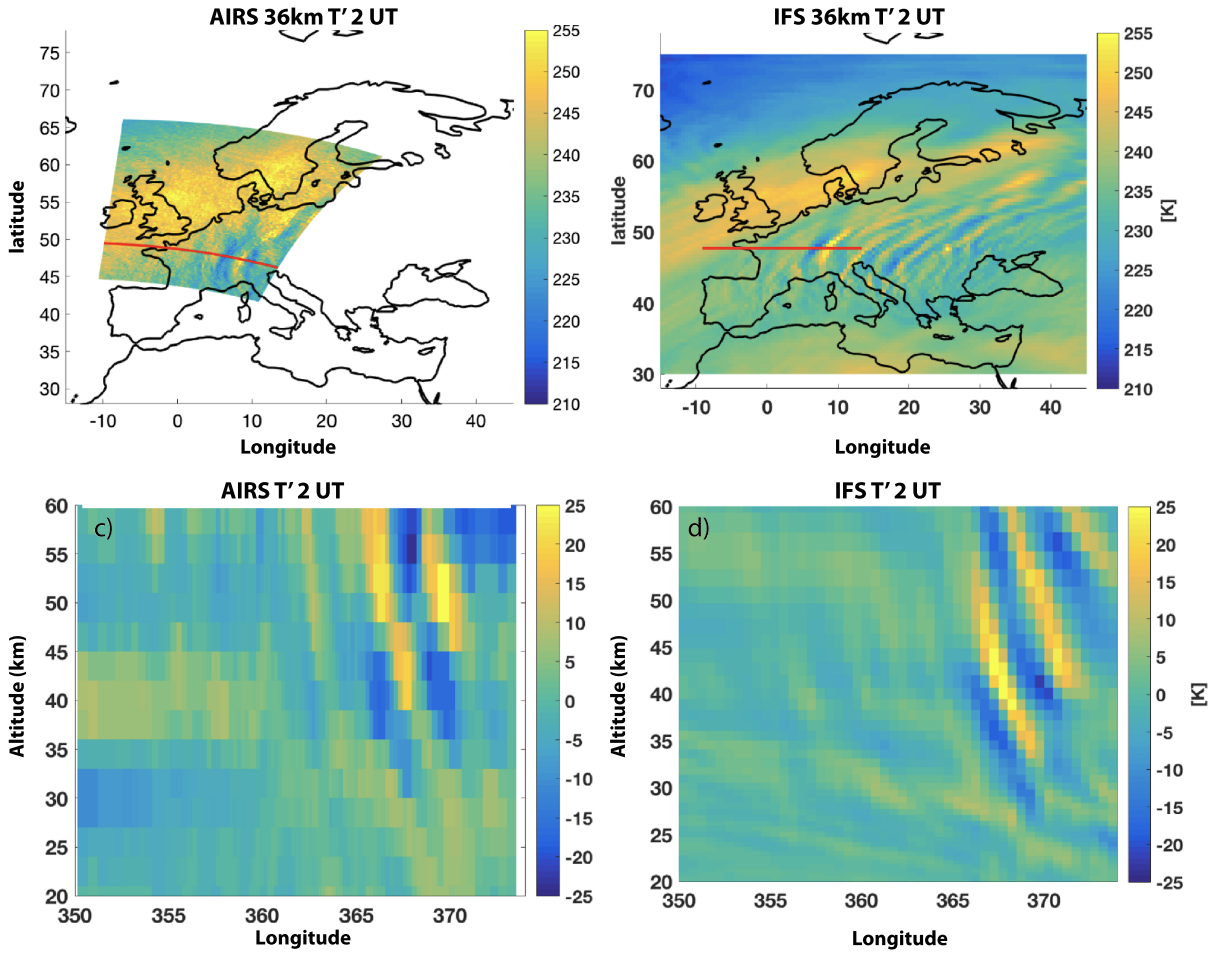

Figure 1. Observations and mesoscale modeling of a mountain wave over Europe on 12 January 2016 for (a) and (b) the AIRS and IFS temperature data at z = 36-km altitude and (c) and (d) a zonal slice of T′ along the red line in the stratosphere.

by the breaking mountain wave. The paper is structured as follows: Section 2 presents the observations and mesoscale modeling of the mountain wave, section 3 presents the numerical model and simulation setup, section 4 presents the results of the simulations, and section 5 serves as summary and conclusions.

2. Observed Mountain Wave

A strong mountain wave was observed by the Atmospheric Infrared Sounder (AIRS) instrument (Aumann et al., 2003) over Central Europe on 12 January 2016. A high-resolution temperature retrieval for this case was obtained using the approach of Hoffmann and Alexander (2009). The AIRS retrieval results at z = 36 km are displayed in Figure 1a and show the wave predominately over the European alps between 5°-10° east and 40°-50° north with a horizontal wavelength of ~230 km. A temperature cross-section, along the red line in Figure 1a, is shown in Figure 1c. The retrieval yielded a wave amplitude of 25 K in the stratosphere and lower mesosphere and a vertical wavelength of ~20 km. One hourly operational analyses and short-term forecasts of the European Centre for Medium-Range Weather Forecasting (ECMWF) provided mesoscale and large-scale modeling results of the event. The integrated forecast system (IFS) of the ECMWF is a global NWP model solving the hydrostatic primitive equations. The horizontal resolution of the IFS cycle used for this study is about 9 km (Hólm et al., 2016; Malardel & Wedi, 2016). Ehard et al. (2018) analyzed ground-based lidar measurements from December 2015 and showed that the IFS data give reliable gravity wave amplitudes up to about 40- to 50-km altitude. During the same period, the phase and location of mountain wave-induced polar stratospheric clouds above Svalbard was very well simulated (Dörnbrack et al., 2017).

Temperature perturbations calculated in a similar manner as for AIRS observations found the presence of a mountain wave with similar amplitudes and wavelengths to the AIRS observation (Figures 1c and 1d). Both showed large temperature enhancements associated with the presence of the stratospheric jet stream to the north of the mountain wave over the United Kingdom and Scandinavia. The IFS data suggest the jet stream causes a refraction of the mountain wave phases from the north-south to the east-west direction, since the horizontal wind is larger north of the wave event. The observation and modeling results, however, do not capture the significant wave nonlinearity and breaking that would be expected from such a strong wave in the Mesosphere and Lower Thermosphere (MLT) region. Therefore, the MAGIC model is used to simulate the mountain wave, along the red line (at 47° N), from the ground up to 300-km altitude in order to examine the breaking processes and nonprimary wave generation associated with this mountain wave event in the upper atmosphere.

3. Numerical Model

The numerical model, used for the simulations, is a 2D version of the time-dependent, high-resolution numerical model, known as MAGIC (Snively, 2013; Snively & Pasko, 2008; Zettergren & Snively, 2015). The numerical model solves the nonlinear, fully compressible Euler equations, with gravity as a balanced source term, and Navier Stokes viscosity (Snively, 2013; Snively & Pasko, 2008). This is done using an adaptation of the Clawpack routines (www.clawpack.org), which solve a hyperbolic system of equations using a finite volume approach (LeVeque, 2002; LeVeque & Berger, 2004). The model decomposes flux differences between cell boundaries into characteristic "f-waves" (Bale et al., 2002), each of which propagate at characteristic speeds. The model accounts for dissipation due to molecular viscosity and thermal conduction and solves for these using a time-split method.

3.1. Wave Forcing and Simulation Domain

The mountain wave is excited using the simplified source used in Heale et al. (2017), which represents the wave as a vertical body forcing with a fixed horizontal phase. Tests were run using a topographic source, but low frequency modes with long horizontal wavelengths were generated that interfered with the side boundary and did not contribute to the solution in the upper atmosphere (our region of interest). Therefore, the simplified source was used. The vertical body forcing is specified as follows:

$$F(x,z,t) = A \cdot \rho \cdot \cos[k(x-x_c)] \cdot \exp\left[-\frac{(z-z_c)^2}{2\sigma_z^2} - \frac{(x-x_c)^2}{2\sigma_x^2} - \frac{(t-t_c)^2}{2\sigma_t^2}\right], \quad (1)$$

where $A = 0.1$ m/s^2, ρ is the density, k is the horizontal wavenumber ($2\pi/230$ km), $z_c = 10$ km, $\sigma_z = 3$ km, $x_c = 1,500$ km, $\sigma_x = 230$ km, $t_c = 6$ hr, and $\sigma_t = 1.5$ hr. The vertical half-width is chosen to be large enough to generate a coherent gravity wave and not so large that the ambient atmospheric conditions vary too rapidly over that scale. The temporal half-width is chosen to ramp the wave up slowly enough that the forcing does not produce large transients. The horizontal wavelength was chosen from the wavelength measured in the AIRS image (230 km). It is noted that IFS applies a sponge layer that artificially decreases amplitudes above ~40-km altitude. In addition, the AIRS retrieval algorithm uses a series of weighting functions at different altitudes (Hoffmann & Alexander, 2009), which also underestimate amplitudes, especially above ~50 km and for waves with short vertical wavelengths. As such, the forcing amplitude was chosen to best match the AIRS and IFS amplitudes in the stratosphere at 40 km where we have more confidence in their accuracy. The simulation domain was chosen to represent a zonal slice at a latitude of 47° north, corresponding to the strongest portion of the wave in Figure 1. The horizontal domain is 3,000 km in zonal extent with a horizontal resolution of 1 km. The vertical domain ranges from the ground to 300-km altitude with 250-m resolution. The simulation was run for 9 hr, with frames output every 2.5 min. The side and top boundary conditions are open, the bottom boundary is closed (reflective), and a sponge layer is applied to the top 30 km of the domain.

3.2. Background Atmosphere

The simulation requires a fixed background ambient atmosphere for the excited mountain wave to propagate through. However, the tidal phase would change significantly over the 9-hr period of the simulation. Therefore, two simulations are run with opposing tidal phases to ascertain some of the differences that would arise from the changing tide that is not captured in the model. The two simulations are named the 2 UT and 7 UT simulations as these represent the times at which the background atmospheric profile was chosen. The atmospheric background zonal winds and temperatures are obtained from the IFS atmospheric

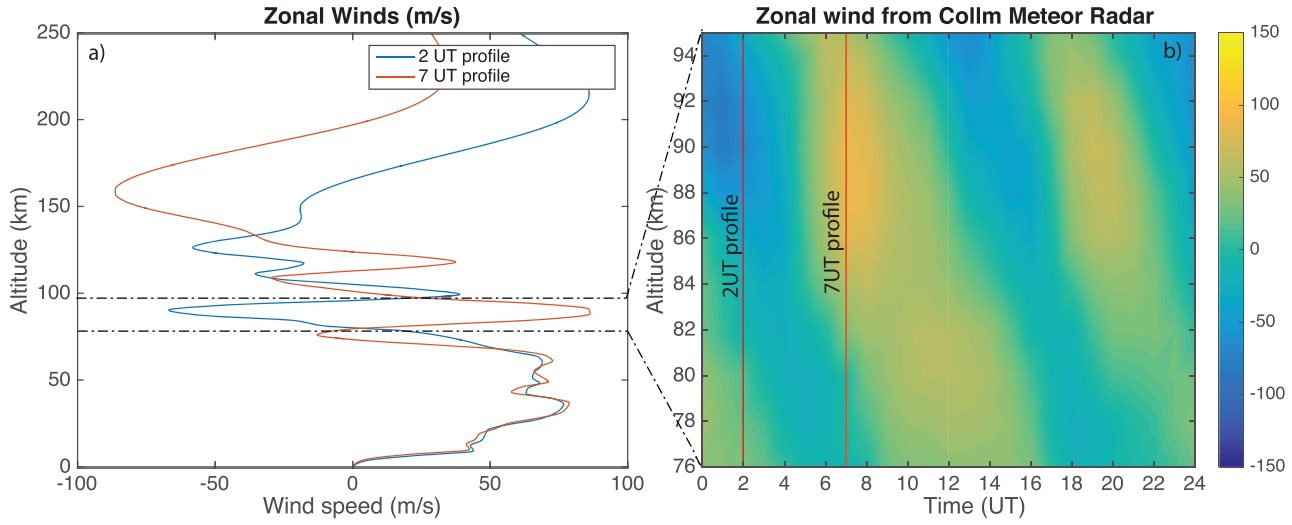

Figure 2. (a) Zonal wind profiles used as background atmospheric conditions for the 2 UT and 7 UT simulations and (b) the Collm Meteor Radar data (m/s) for 12 January 2016.

states for z = 0–60 km altitude. The meteor radar at Collm, Germany (51.30° N, 13.02° E) (Jacobi, 2012; Stober et al., 2017), was used to represent the winds between 70 and 100 km and captures the tidal phases (Stober et al., 2018), and the HWM07 model (Drob et al., 2008) was used for the winds above 100 km and between 60 and 70 km. The temperature and densities were taken from NRLMSISE-00 model (Picone et al., 2002). The zonal wind profiles for the 2 UT and 7 UT simulations are shown in Figure 2a, with the Collm meteor radar (MR) winds shown in Figure 2b.

Figure 2a indicates that the lower atmospheric winds (0–60 km) show little variation between 2 and 7 UT but have opposing tidal phases between 70- and 100-km altitude (westward at 2 UT and eastward at 7 UT). The eastward tide in the 7 UT simulation has a larger magnitude than the westward tide at 2 UT by ∼20 m/s. The thermospheric winds are also significantly different at 2 and 7 UT with the winds predominantly eastward at 2 UT (peaking at 210-km altitude) and westward at 7 UT (peaking at 160-km altitude).

4. Effects of Atmospheric Wind and Temperature on Waves

In order to understand the discussion in the results section, a brief description of the effects of winds and temperature structure on waves is presented here. Horizontal winds and temperature structure that vary in altitude refract a wave by changing the vertical wavelength. If the wind increases in the direction of wave propagation, then the wave's vertical wavelength is decreased and the wave's trajectory becomes more horizontal; a positive temperature gradient with altitude will have the same effect. If the wind increases in the opposite direction of the wave propagation, the vertical wavelength is increased and the wave's trajectory becomes more vertical; a negative temperature gradient with altitude will have the same effect. If the wind is in the same direction as the wave and increases to the point where its magnitude matches the horizontal phase speed of a wave, the vertical wavelength approaches zero and the wave is absorbed into the mean flow (a critical level). Often times, if the wave is of sufficient amplitude, the refraction to small vertical scales leads to large vertical shears in the wave itself, which can cause the wave to break as it approaches a critical level. If the winds and temperature structures vary such that the wave's intrinsic frequency becomes equal to the local buoyancy frequency, then the wave will undergo partial or total reflection. The region above the reflection layer is known as an evanescent region (region where the buoyancy period exceeds the wave period), where the wave solution decays exponentially with altitude. However, with sufficient amplitude, the wave can tunnel through the evanescent layer and continue propagating above the upper edge of the layer. In the context of these simulations, the strong tidal winds can act as a critical or evanescent layer for certain wave modes, depending upon the wave parameters and their direction of propagation. Therefore, the tidal phase shown in Figure 2b has the ability to control the spectrum of waves that can propagate into the upper regions of the thermosphere.

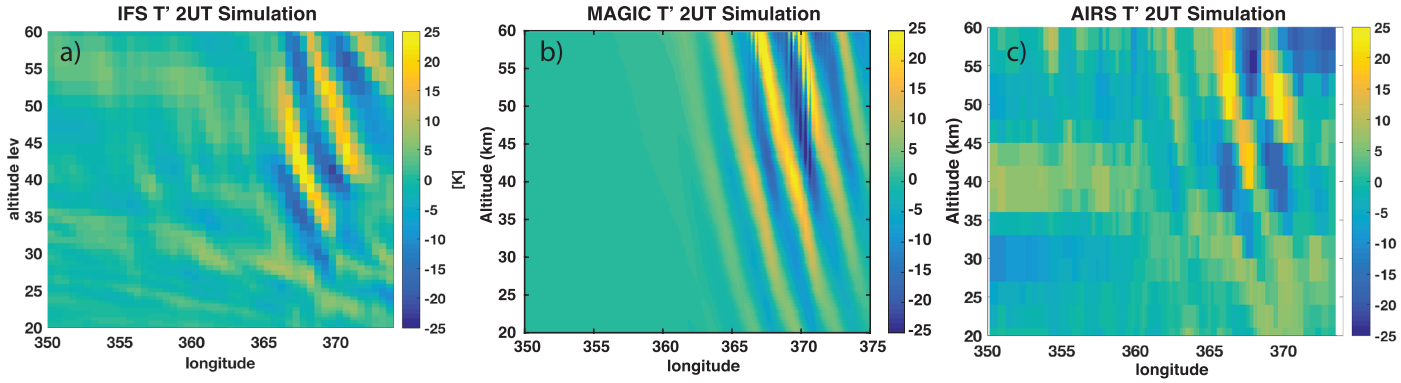

Figure 3. Comparison of the zonal-altitude slices for the (a) IFS, (b) MAGIC, and (c) AIRS temperature perturbations in the stratosphere (K).

5. Results

5.1. Comparison with AIRS and IFS

Figure 3 shows a comparison of the zonal-altitude slice at 47° north in the AIRS observation, MAGIC simulation, and the IFS. The MAGIC model (Figure 3b), even with the simplified source, captures the amplitudes and vertical phase structure of the mountain wave well when compared with Figures 3a and 3c . As previously noted, the MAGIC amplitudes were chosen so that they match well with IFS and AIRS at 40-km altitude. Above this altitude, the IFS and AIRS results may underestimate the true amplitude of the wave due to sponge layer damping and larger uncertainties in the retrieval algorithms, respectively. However, tests with MAGIC suggest that the wave is already close to saturation at the amplitude shown in Figure 3b. Increasing the amplitude of the forcing even more will lead to increased linearities and harmonic generation but will not impact the primary wave amplitudes much. Making this comparison gives us confidence (1) in using the simplified source and (2) that the results in the MLT are a fair representation of the actual dynamics that would occur in 2D. Note that amplitudes and breaking dynamics would be different in 3D and will be examined in a future paper.

5.2. Wave Evolution

Figure 4 shows the temperature perturbation field, for both the 2 UT (a-c) and 7 UT (d-f) simulations, at $t = 5.83, 6.6$, and 7.5 hr into the simulation . At $t = 5.83$ hr (panels a and d), the mountain wave can be seen clearly in the lower and middle atmosphere but does not propagate above the red dotted line, which represents the lowest altitude that the zonal wind crosses zero. The point where the zonal wind (represented by the blue line in Figure 4) crosses zero is a critical level for mountain waves (since a stationary mountain wave possesses a zero ground-relative phase speed). As the mountain wave approaches the critical level, the decreasing wind causes the vertical wavelength of the wave to decrease in tandem. The decreased vertical wavelength leads to larger vertical gradients in the wave fields, which can cause a wave to break as it approaches the critical level. Since the lowest critical level exists at 80 km for the 2 UT simulation and 73 km in the 7 UT simulation, the mountain wave can propagate higher before it is likely to break in the 2 UT case. It also means that the horizontal phase structure is different at the altitude the wave breaks in the 2 and 7 UT cases.

At $t = 6.6$ hr (Figures 4b and 4e), the mountain wave breaks into smaller structure above ~60 km as it approaches the critical level (indicated by the red dotted line) and the vertical gradients in the wave become large enough to cause instability. Due to the phase progression between the different breaking altitudes in the 2 and 7 UT simulations, the mountain wave breaks along two wavefronts in the 2 UT simulation (Figures 4b), and three wave fronts in the 7 UT simulation (Figures 4e). The breaking is most prominent in the warm phase of the wave as instability conditions are more likely to be met here (see Heale et al., 2017 for more details). Nonstationary nonprimary waves are present above ~100-km altitude in both Figures 4b and 4e (see the supporting information for the movie), generated by the breaking of the mountain wave. In Figures 4b, there are two very distinct packets of nonprimary waves at 368° and 372° longitude that are propagating eastward. In Figures 4e, there is one, broader, region of nonprimary waves spanning ~368°-371°, which propagate in both eastward and westward directions. The strong wind associated with the tide at 90-km altitude can act to critical level filter waves propagating in the direction of the wind (or lead to significantly slower wave

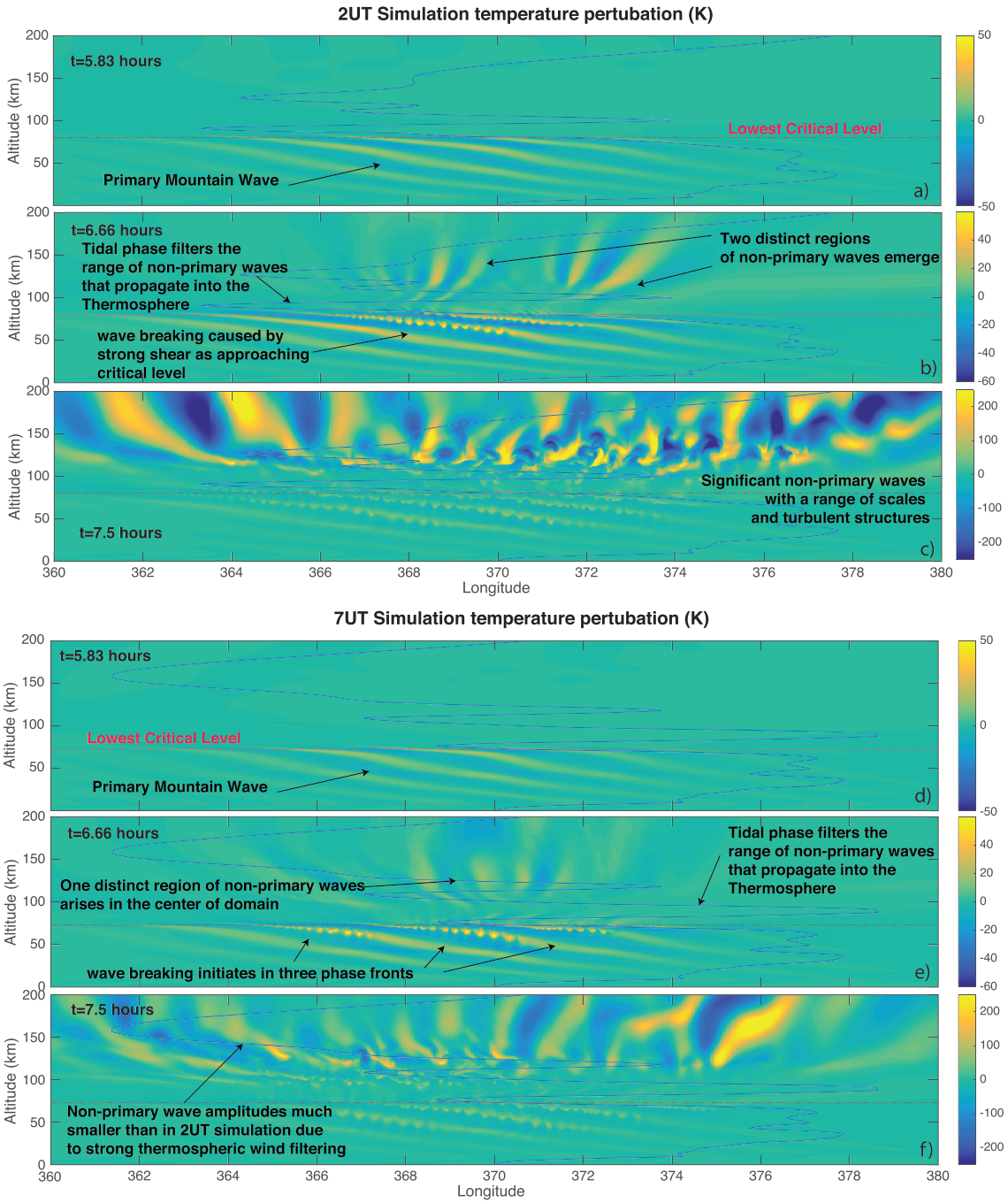

Figure 4. Temperature perturbation field at t = 5.83, 6.6, and 7.5 hr for the (a,b,c) 2 UT simulation and (d,e,f) 7 UT simulation. The horizontal red dotted line represents the lowest critical level the mountain wave encounters and the blue line represents the structure of the zonal wind.

modes) and can cause reflection and evanescence of waves propagating against the wind (leading to rapidly decaying vertical aligned phase fronts). Either way, the amplitudes are diminished in this region as a result. Thus, the tidal wind acts as a filter, controlling which nonprimary waves can propagate from the breaking region to the thermosphere as noted previously by Becker and Vadas (2018). It is noted, however, that the wind is time invariant in these simulations and that hard critical levels and turning point levels become more transient when time dependence is included (e.g., Broutman & Young, 1986; Eckermann, 1997; Heale & Snively, 2015; Senf & Achatz, 2011).

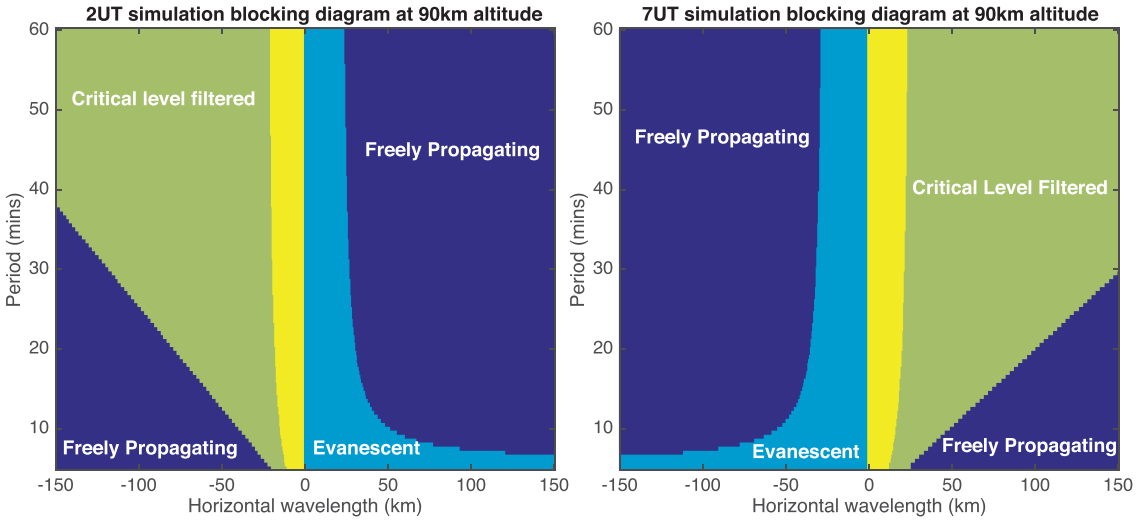

Figure 5. Blocking diagram showing the wavelength-period combinations for AGWs, which are freely propagating, critical level filtered, or evanescent at 90-km altitude where the tidal wind is strongest. The 2 UT simulation blocking diagram is shown on the left and the 7 UT on the right.

At $t = 7.5$ hr (Figures 4c and 4f), nonprimary waves, at a range of scales, are dominant in the thermosphere (above 100 km) with amplitudes of up to 250 K. The initial nonprimary waves, seen in Figures 4b and 4e, undergo further breaking and turbulence particularly at ~130-km altitude leading to further wave generation. Vadas and Becker (2019) show a similar scenario in their GCM simulations of mountain wave breaking over the Andes. They find that primary mountain waves breaking between 60 and 80 km that generates secondary waves that are then dissipated around 110-km altitude generate a further body force and produce tertiary waves. However, the scales are very different in their study. In this study, we use the generic term nonprimary to refer to any wave that is not the primary mountain wave so we do not have to keep count of the level of wave generation (secondary, tertiary, etc.). The differences in thermospheric wind in the 2 and 7 UT simulations cause noticeable differences in the nonprimary wave dynamics in this region. In the 2 UT simulation (Figures 4c), waves propagate both eastward and westward, with the eastward propagating waves prone to breaking, while the westward propagating waves propagate more freely. In the 7 UT simulation (Figures 4f), westward propagating waves are severely filtered or damped by the strong westward wind, leaving the eastward propagating waves to possess the largest amplitudes. This shows the importance of understanding the nature of the thermospheric wind in determining the propagation and dissipation of nonprimary waves in this region. Please see the supporting information for movies showing the evolution of the two wave fields.

5.3. Tidal Filtering

Figure 5 shows a diagram of the horizontal wavelength and period combinations of AGWs that will be critical level filtered, evanescent, or freely propagating at 90-km altitude where the tidal wind is at its maximum amplitude. The primary mountain wave breaking occurs below this altitude and the non-primary waves are dominant above. The tidal wind then acts as a filter to allow certain modes to propagate from the mesosphere up into the thermosphere. For the 2 UT simulation, the tidal wind peaks at a westward amplitude of 65 m/s while it peaks at an eastward amplitude of 85 m/s for the 7 UT simulation. Thus, waves with horizontal phase speeds less than these respective winds will be critical level filtered (for waves propagating in the direction of the wind). For waves propagating against the wind, all wavelengths shorter than ~40 km are likely to be evanescent. It can be seen from Figure 5 that there are a broader range of waves that can freely propagate against the tide than with it and that a broader range of scales can propagate in the 2 UT case than the 7 UT case.

5.4. Association Between Initial Wave Breaking, Wave Forcing, and Nonprimary Waves

In this subsection, we explore the connection between the breaking scales of the wave, the localized forcing created by momentum deposition associated with the breaking, and the generation of nonprimary waves. In particular, we look at the onset of breaking and the initial nonprimary waves that are created. In order to analyze the localized forcing, we calculate the horizontal and vertical forcing as defined in Zhou et al.

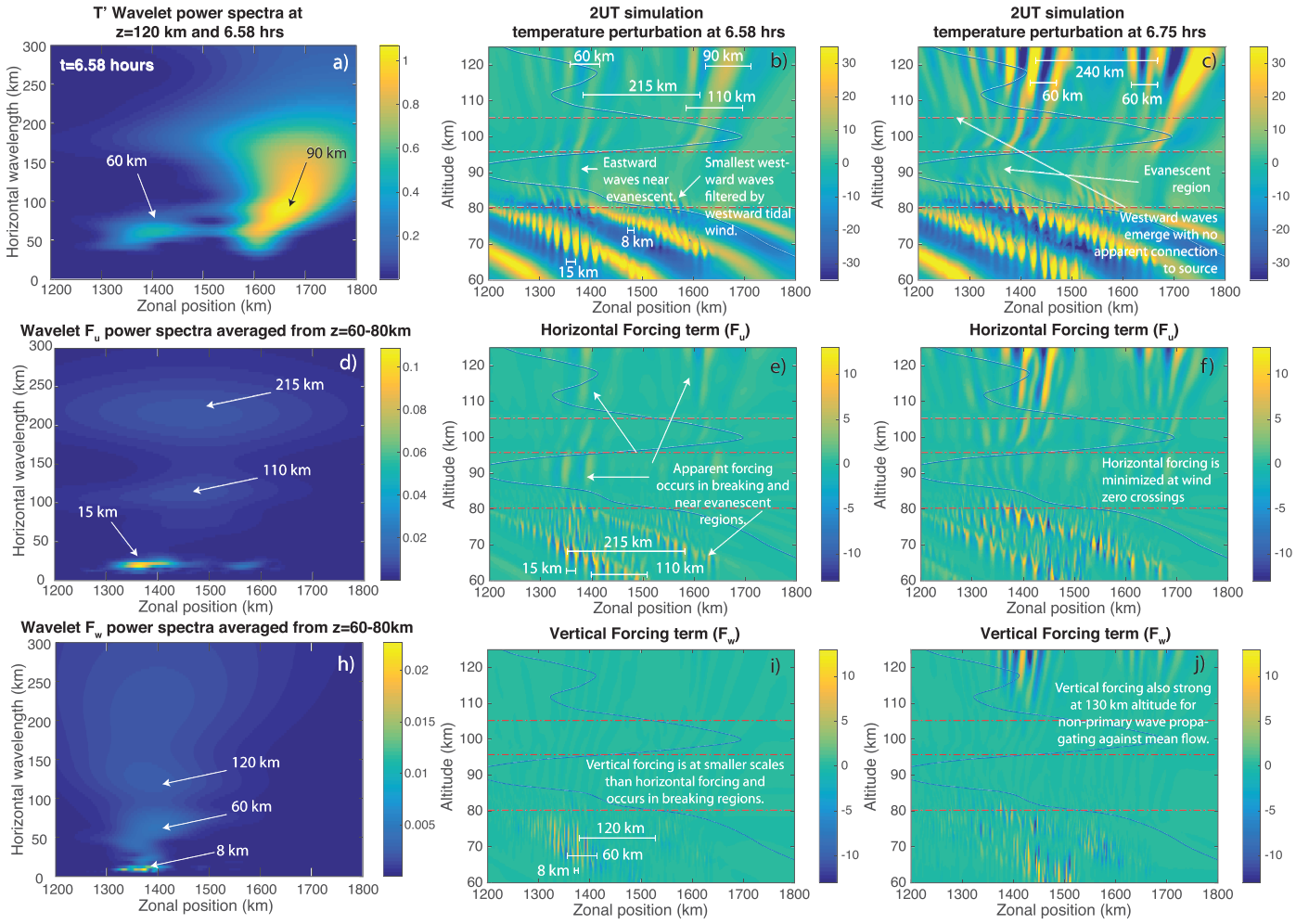

Figure 6. The temperature perturbation (K) (b,c), horizontal forcing term ($F_u(m/s^2)$) (e,f), and vertical forcing term ($F_w(m/s^2)$) (i,j) at $t = 6.58$ and 6.75 hr for the 2 UT simulation. The left hand panel shows a wavelet transform of (a) the temperature at $z = 120$ km, highlighting the propagating nonprimary wave scales, (d) the horizontal forcing scales averaged from 60 to 80 km, and (h) the vertical forcing scales averaged from 60 to 80 km.

(2002) and also used in Chun and Kim (2008).

$$F_u = -\frac{1}{\rho_0}\frac{\partial}{\partial x}(\rho_0 u'^2) - \left[-\frac{1}{\rho_0}\frac{\partial}{\partial z}(\rho_0[u'w' - \overline{u'w'}])\right], \tag{2}$$

$$F_w = -\frac{1}{\rho_0}\frac{\partial}{\partial x}(\rho_0 u'w') - \frac{1}{\rho_0}\frac{\partial}{\partial z}(\rho_0[w'^2 - \overline{w'}]). \tag{3}$$

It is noted, however, that Chun and Kim (2008) states "these terms do not solely represent the momentum due to breaking of the primary waves. Rather, it represents simply a nonlinear forcing for the linear gravity waves. The magnitude of the nonlinear forcing is directly related to the magnitude of the perturbations that represents waves, thus they are not completely separable."

Figures 6 and 7 show the temperature perturbations at $t = 6.58$ and 6.75 hr and the corresponding horizontal and vertical forcing at each of those times for the 2 UT and 7 UT simulations, respectively. A Morlet wavelet transform (Torrence & Compo, 1998) is used to examine the spatial spectrum of the temperature at $z = 120$ km in panel a (representing the initial nonprimary waves) and of the horizontal and vertical forcing from 60- to 80-km altitude in panels d and h (the spectrum is averaged over this altitude and represents the primary wave breaking region).

Figures 6b and 6c show that wave breaking occurs between 60- and 80-km altitude and is most visible within the warm fronts of the wave in the 2 UT simulation. The horizontal scales of the turbulent eddies in Figure 6b

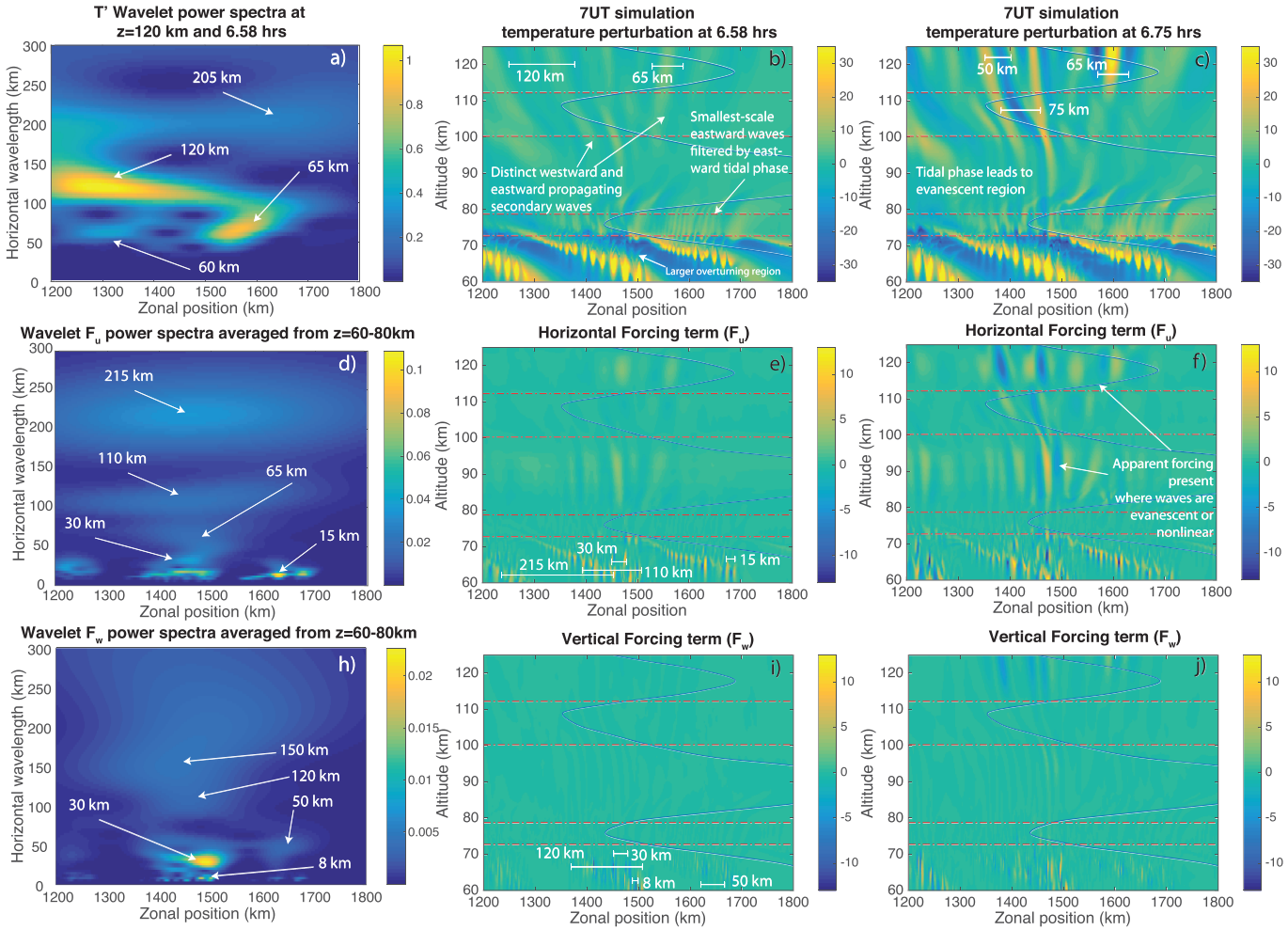

Figure 7. The temperature perturbation (K) (b,c), horizontal forcing term ($F_u(m/s^2)$) (e,f), and vertical forcing term ($F_w(m/s^2)$) (i,j) at $t = 6.58$ and 6.75 hr for the 7 UT simulation. The left hand panel shows a wavelet transform of (a) the temperature at $z = 120$ km, highlighting the propagating nonprimary wave scales, (d) the horizontal forcing scales averaged from 60 to 80 km, and (h) the vertical forcing scales averaged from 60 to 80 km.

range from 8 and 15 km and occur along two of the mountain wave phase fronts. Nonprimary waves can clearly been seen, just above the lowest red dotted line in panels b and c, emanating from the breaking region at those same eddy scales. However, nonprimary waves at these scales cannot propagate above the tidal wind at 90-km altitude due to critical level filtering or reflection (depending upon the propagation direction). There are two distinct regions of nonprimary waves that propagate (eastward) beyond the tidal winds at 90 km into the thermosphere, which originate from each of the two breaking phase fronts (located at x~1,350 and 1,550 km in Figures 6b and 6c). The most western packet of nonprimary waves (at $x = 1,300$–1,400 km in Figures 6b and 6c) has a dominant horizontal scale of 60 km at 120-km altitude (as labeled in Figure 6a) and are evanescent while propagating through the tidal wind field but tunnel through this region and can emerge above leading to both eastward and westward propagating waves. The eastern packet of nonprimary waves ($x = 1,600$–1,700 km in Figures 6b and 6c) have a broader range of horizontal scales from 50 to 180 km, with peak power at 90 km (also labeled Figure 6a).

The second row of Figure 6 shows the horizontal forcing (F_u, panels e and f) and its wavelet spectrum averaged over 60- to 80-km altitude (panel d). Three dominant horizontal forcing scales arise at 15, 110, and 215 km in panel d. The 15-km horizontal forcing in Figure 6d corresponds to the prominent eddy scales seen in Figures 6b and 6c and produces nonprimary waves that are filtered by the tide. The 110-km forcing in Figure 6d corresponds to the horizontal width of one of the breaking phase fronts (labeled in panel e), while the 215-km scale, in Figure 6d, corresponds to the distance between the two breaking mountain wave phase fronts (also labeled in panel e). Weak horizontal forcing is also present in the westward winds in the

thermosphere (for eastward propagating waves), due to evanescent decay of the wave and due to nonlinear forcing in the regions above 110-km altitude. It is noted that the apparent forcing in the evanescent is not a body forcing as would occur for wave dissipation by viscosity/conduction or a forcing as produced by breaking. Rather, the apparent vertical momentum flux divergence is associated with the exponential decay that occurs in an evanescent region. The 110-km scale forcing, in Figure 6e, leads to the approximate packet scale of each of the two nonprimary wave regions in panel b and the 215-km scale produces the spacing between these two nonprimary wave regions.

The third row of Figure 6 shows the vertical forcing (F_w, panels i and j) and its wavelet spectrum averaged over 60- to 80-km altitude (panel h). The dominant scale of this forcing labeled in panel i, at 8 km, is much smaller than the horizontal forcing in panel e. This 8-km scale forcing clearly couples to nonprimary gravity waves (Figure 6b at $x = 1,550$ km, $z = 80$ km); however, these waves cannot propagate above the strong tidal wind at 90-km altitude. The wavelet spectra (panel h) also shows power at 40- to 90- (peaking at 60 km), 120-, and 240-km horizontal scales. The 40- to 90-km horizontal scale arises from the widths of the vertical forcing within one breaking mountain wave front and the larger scales arise from the forcing associated with the breaking between two mountain wave phase fronts (labeled in panel i). The 60- to 90-km horizontal scales of vertical forcing in panel i correspond to the dominant nonprimary waves seen propagating at 120-km altitude in panels b and c. The evidence in this figure, while showing correlation rather than causation, suggests that the horizontal forcing contributes to packet scales of the nonprimary waves, while the vertical forcing helps govern the horizontal wavelength of the propagating waves shortly after the onset of breaking.

Figure 7a shows significant nonprimary wave power at horizontal scales between 60 and 120 km. These scales are similar to those observed in Figure 6a; however, the nonprimary wave regions are not as distinct and propagate in both eastward and westward directions. As mentioned previously, three phase fronts can be seen breaking in panel b of the 7 UT case as opposed to two in panel b of the 2 UT case. As with the 2 UT case, the smallest scales of breaking generate waves that are filtered or reflected by the tidal wind.

In the second row of Figure 7 (horizontal forcing), notable scales of horizontal forcing are seen at 15, 30, 65, 110, and 215 km in panel d. The 15-, 110-, and 215-km modes are the same as those seen in the 2 UT case and are defined by the breaking scales, mountain wave phase front scale, and mountain wave horizontal scale, respectively. However, the 30- to 65-km scales in panel d are not present in the 2 UT simulation and appear to arise from a larger overturning region formed between two vertical phases of the wave in the middle of the domain (labeled in panel b). The 60- to 65-km scale transfers into nonprimary propagating waves that are dominant at 120-km altitude in panels b and c, while the 30-km mode is filtered.

Figure 7h (vertical forcing) displays prominent scales of 8 and 30 km with a weaker mode at 50–60 km and a continuum of scales from 100 to 250 km (with relative peaks at 120 and 150 km). The 8- and 30-km modes are filtered or evanescent over the region dominated by the tidal wind at 90-km altitude. The larger scale modes, particularly at 60 and 120 km, appear to couple efficiently in to propagating nonprimary waves (seen at $z = 120$ km in panel c) at these early onset breaking stages and are defined by the widths of vertical forcing within one breaking mountain wave phase front.

Since Figures 6 and 7 show the early stages of breaking, and most phase lines can be traced to the source region, it is suggested that most of the waves seen here are nonprimary waves connected to the initial mountain wave breaking. However, some waves emerge above 100-km altitude, with both westward and eastward propagation directions, that have no direct phase lines connected to the source region. The presence of evanescence and tunneling in both the 2UT and 7UT cases complicates the connection between the waves generated by the breaking of the mountain wave and the propagating nonprimary waves in the upper thermosphere. The westward and eastward waves could simply be the emergence of "waves" that tunnel through the evanescent region and continue to propagate according to the local wind and shear as they emerge. However, it could also be the case that some of the waves are generated by further wave dissipation as described by Vadas and Becker (2019). In this mechanism, initial nonprimary waves are further dissipated or break (between 80 and 130 km, peaking at 110 km in their study), which generates body forces that produce further waves. This mechanism can continue multiple times producing additional nonprimary waves. It is certainly the case that the further breaking of nonprimary waves occurs at later times, as seen in Figures 4c and 4f between 100- and 150-km altitude. It is unclear how much this mechanism contributes to the propagating nonprimary waves versus those that tunnel through the evanescent layer or from direct propagation.

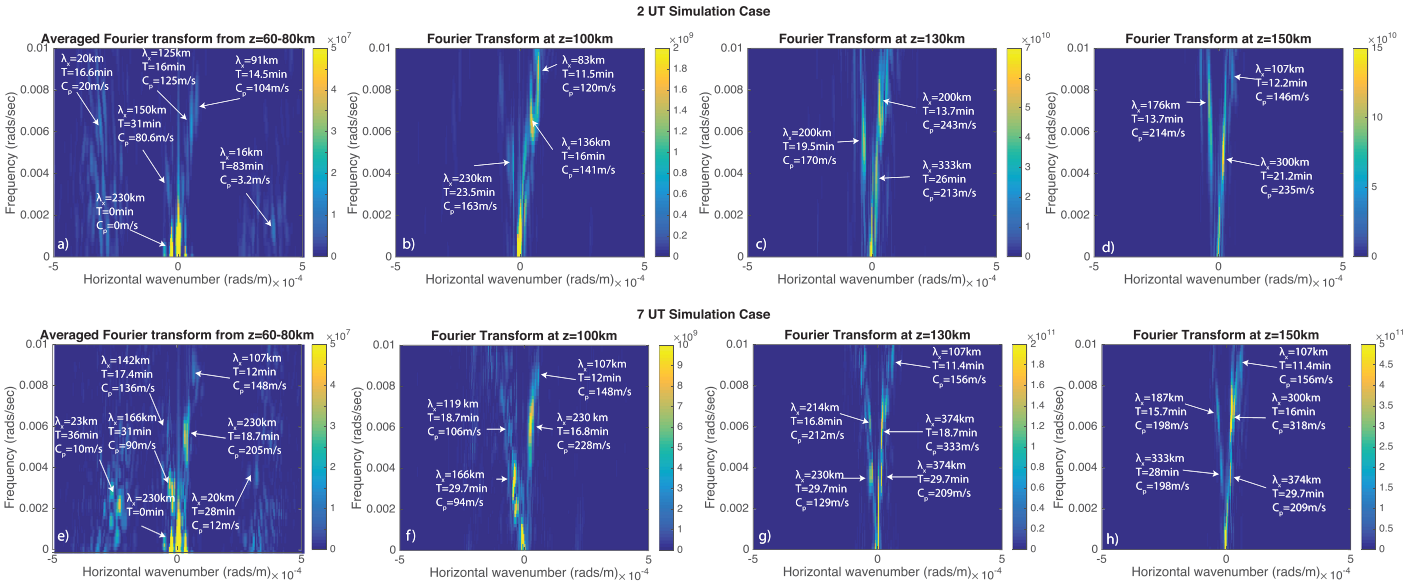

Figure 8. Fourier transform of the temperature perturbation for (a-d) the 2 UT simulation and (e-i) the 7 UT simulation at 60-80 (averaged), 100, 130, and 150 km altitude.

5.5. Nonprimary Wave Spectra

In the previous subsection, the breaking scales, resulting forces, and coupling to the initial nonprimary wave scales was examined. In this subsection, the periods and scales of the waves are examined over the entire duration and domain of the simulation. As such, these spectra contain the mountain wave, and all nonprimary waves. Figure 8 shows the Fourier transform of the temperature perturbation at 60- to 80- (averaged), 100-, 130-, and 150-km altitude for both the 2 UT and 7 UT simulations.

Figures 8a and 8e show the scales and periods of the waves associated with the primary mountain wave and those generated by its breaking and nonlinearity. With the exception of power at the zeroth order, the strongest mode is the mountain wave (230 km, 0 period). The small-scale breaking scales (8–30 km) that are seen below the first red dotted line in Figures 6b and 7b are present in the spectra in Figures 8a and 8e but are not particularly strong relative to the mountain wave. Waves generated at these scales and periods have very slow phase speeds (~10 m/s), which is why they are easily filtered out by the tidal winds and do not appear in the spectra at 100-, 130-, or 150-km altitude.

In the 2UT simulation, three distinct regions of wave power are observed over the 60- to 80-km altitude region, in Figure 8a, which are centered at 150 km and 31 min (propagating westward), 125 km and 16 min, and 91 km and 14.5 min (propagating eastward). At 100-km altitude, in Figure 8b (above the strong tidal wind phase), there are still three distinct modal regions, but the central wavelength and periods change to 230 km and 23.5 min (westward propagating), 136 km and 16 min, and 83 km and 11.5 min (eastward propagating), respectively. The 136-km and 16-min period dominant mode seen in Figure 8b can be correlated to a corresponding mode in Figure 8a, at $z = 60$–80 km (centered at 125 km and 16 min), but it is difficult to draw any strong conclusions between the relationship of the other regions other than they share similar periods. The central wavelength and periods change again at both 130 and 150 km, in Figures 8c and 8d, respectively, but the following general trends are true: The eastward mode has the strongest spectral amplitude, there are two distinct modal regions eastward and one westward, the spectra becomes more bandwidth limited in wavelength, but more diffuse in period, as the altitude increases. This occurs because the increasing viscosity with altitude preferentially damps smaller scales and "smooths" wave modes to remove discrete turbulent-like features. The phase speeds in the thermosphere are in the 150–250 m/s range.

In the 7 UT simulation case, over the 60- to 80-km altitude region (Figure 8e), there is one dominant westward propagating mode (166 km and 31 min) and one dominant eastward propagating mode (230 km, 18.7 min) with two weaker modes present as well (142 km, 17.4 min, westward; and 107 km, 12 min, eastward). Unlike in the 2 UT case, the spectral periods at $z = 100$ (Figure 8f), 130 (Figure 8g), and 150 km (Figure 8h) correspond fairly well to the spectral periods over 60–80 km (Figure 8e). A strong case could be

made that the nonprimary wave modes seen in the thermosphere are a direct result of the modes arising from the breaking and nonlinearity of the mountain wave in the mesosphere.

However, the situation is complicated by the fact that there is more than one level of breaking as can be seen in Figures 4c and 4f. Therefore, waves in the upper atmosphere could be generated by multiple levels of breaking and new wave production (Vadas & Becker, 2019). It is difficult to trace the origins of spectral components in the thermosphere directly to regions in the primary wave vicinity. In addition, the strongest wave modes at $z = 150$ km have a horizontal scale larger than the primary wave (300 km) in both the 2 UT and 7 UT simulations. Theory suggests that wave breaking produces scales and periods that are smaller and faster than the primary wave mode (Kim & Chun, 2008), while packet scale dissipation (for a single packet) creates body forces that produce waves with larger scales and longer periods than the primary wave (Vadas et al., 2018). The latter mechanism is better suited to explaining the large wave scales dominant at 150-km altitude; however, the periods are 16 and 22 min, respectively, which are much much shorter than the quasi-stationary primary mountain wave. Vadas and Becker (2019) a found that the dissipation of intersecting wave packets can lead to constructive and destructive forcing that generates waves with horizontal wavelengths smaller than the initial packet. It is also noted that very localized forcings (in either space or time) can produce a broad spectra of waves (Heale et al., 2014, 2018), a prominent example of which are convective forcings from individual thunderstorm plumes (Alexander & Holton, 2004; Beres, 2004; Lane et al., 2001). Therefore, localized forcings, such as those that arise from the small breaking scales or constructive/destructive interference of several wave packets, could credibly produce a broad spectra of waves with high temporal variability. This result was also found in Vadas and Crowley (2010) and could explain the relatively short periods of the large scale waves at $z = 150$ km.

5.6. Spatial Distribution of Wave Forcing

In this subsection, the time-averaged forcing magnitude is analyzed for both the 2 UT and 7 UT cases. The quantity analyzed is $F_t = \overline{\sqrt{F_u^2 + F_w^2}}$. where the overline represents the time average over the entire simulation. The time-averaged forcing magnitudes are presented in Figure 9. The first thing to note is that there is a huge difference between the distribution of wave forcing in the thermosphere in the 2 UT and 7 UT simulations. Second, the strongest forcing arises from nonprimary waves that are currently not accounted for in GCMs. This suggests that wave forcing in the MLT and thermosphere are likely significantly underestimated in these models over mountains (Vadas et al., 2019).

In the 2 UT simulation (Figure 9a), the wave forcing is distributed over a fairly broad area in the thermosphere, ranging from 360° to 380° longitude and 100- to 220-km altitude. There are three distinct regions of strong forcing, one is westward of the source and peaks at 150-km altitude and 363° longitude; the other two are eastward of the source with peaks at 130- and 150-km altitude and 372° and 375° longitude. In comparison, the 7 UT simulation (Figure 9b) only displays a region of strong forcing eastward of the source at 150-km and 375° longitude. This difference can be attributed to the differences in the thermospheric wind in both simulations. The strong westward thermospheric wind (which peaks at approximately −90m/s at 160-km altitude) in Figure 9b acts to filter and refract westward propagating waves to smaller vertical scales, which increases the rate at which they are dissipated. Therefore, the westward propagating waves that are present in the 2 UT simulation are removed by filtering and dissipation in the 7 UT simulation. This effect is clearly visible in Figure 4f, the westward nonprimary waves are breaking at ∼130-km altitude where the westward zonal shear is maximized and are reduced to small scales, which are readily dissipated. The eastward waves have much larger vertical scale, can propagate to higher altitudes, and as such obtain larger amplitudes before dissipating. In contrast, the eastward waves in Figure 4c are breaking and have smaller vertical scales than the westward waves due to the wind shear being eastward above ∼130-km altitude. The differences in the eastward forcing in the 2 UT and 7 UT simulations can be attributed to the tidal wind phase at 90-km altitude acting to filter the range of nonprimary waves that can propagate up into the thermosphere. The phase of the 2 UT simulation tide is westward and of smaller magnitude than in the 7 UT simulation. As such, a greater range of eastward propagating nonprimary waves can propagate from the mountain wave breaking region up into the thermosphere in the 2 UT simulation than in the 7 UT simulation where they are filtered by the strong eastward tide.

Figure 9 shows the importance of the tidal phase and thermospheric wind dynamics in governing the wave forcing due to nonprimary waves in the thermosphere. While the primary mountain wave also produces

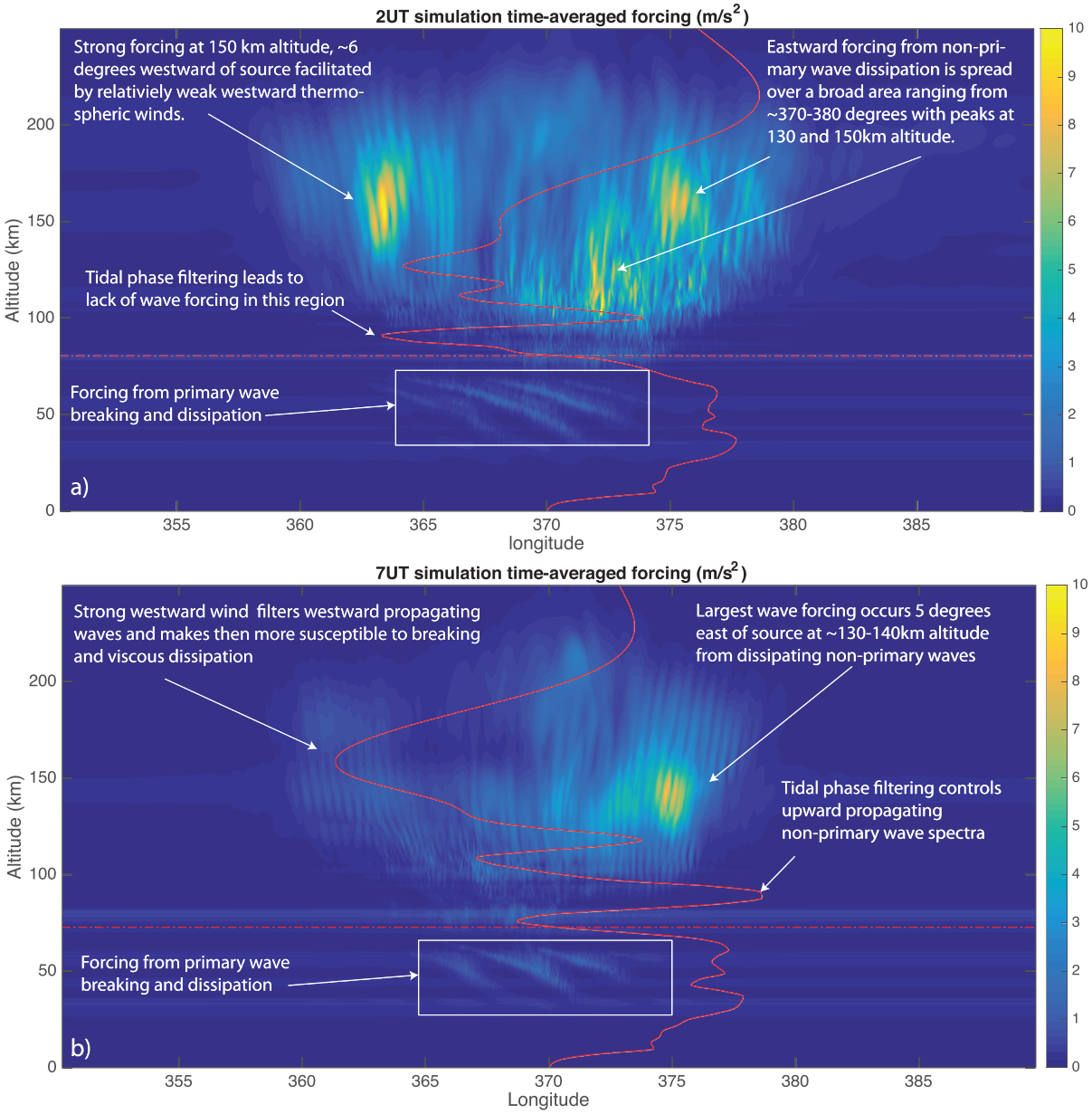

Figure 9. The time-averaged magnitude of the wave forcing for the (a) 2 UT and the (b) 7 UT simulation.

a wave forcing in both simulations, the time averaged amplitude is half that of the peak forcing due to nonprimary waves in the thermosphere.

6. Summary and Conclusions

In this study, we simulated a strong, persistent mountain wave observed over northern Europe on 12 January 2016 using the MAGIC model in 2D. Two simulations were run with fixed background zonal wind structure taken at 2 and 7 UT, respectively, and representing opposing tidal phases. The aim of the study was to investigate the nature of the mountain wave breaking, dissipation, and nonprimary wave generation in the mesosphere and thermosphere with different background wind conditions. The simulations showed breaking of the mountain wave as it approaches a critical level in the mesosphere, which generated a broad range of nonprimary waves that propagated both eastward and westward. The dominant turbulent horizontal scales produced by the breaking mountain wave were between 8 and 30 km, with larger forcing scales defined by the approximate width of the each phase of the mountain wave (~110–150 km) and the

spacing between horizontal phases (~215–250 km). The dominant turbulent scales couple directly to horizontal scales of propagating nonprimary waves; however, these waves are critical level filtered (or rendered evanescent, depending upon direction of propagation) by the strong tidal wind at 90-km altitude and do not propagate up into the thermosphere. The tidal phase and amplitude acts like a filter and controls the spectra of nonprimary waves that can propagate up into the thermosphere. It is noted, however, that if the background winds were time dependent, the amount of critical level filtering and evanescence would likely be reduced. This will be investigated in future studies. The initial nonprimary waves that propagate up into the thermosphere (above 100 km) have horizontal scales between 60 and 120 km with the wave scales influenced by both the horizontal and vertical forcing scales. Over the course of the simulation, the nonprimary waves that are most dominant at 150-km altitude have distinct scales at 107, 170–190, and 300 km with periods of 11–12, 14–16, and 16–22 min, respectively. The phase speeds range from 140 to 318 m/s. It is also noted that the term nonprimary wave is more appropriate than nonprimary wave, since the waves break more than once generating a cascade of scales and periods. The time-averaged wave forcing magnitude resulting from nonprimary wave dissipation and nonlinearity in thermosphere is significant (~2× the forcing from the dissipating primary wave) and peaks between 130- and 150-km altitude. The spatial distribution of wave forcing is heavily influenced by the thermospheric winds. In the 2 UT simulation, wave forcing is strong both eastward and westward of the source and the distribution is broadly spaced as a result of the weaker thermospheric winds between 100- and 150-km altitude. In the 7 UT simulation, strong westward winds and shears lead to filtering, breaking, and dissipation of the westward propagating wind leaving a relatively localized region of strong forcing eastward of the source. Understanding the thermospheric wind dynamics will be crucial to determining the forcing generated by nonprimary waves in the upper atmosphere. Nonprimary waves can contribute significantly to the wave forcing of the upper atmosphere and are currently unaccounted for in the GCM parameterizations. While beyond the scope of this paper, downward propagating nonprimary waves can also reduce the momentum flux in the mesosphere and stratosphere (Chun & Kim, 2008). Taking these processes into account will be crucial to producing more realistic atmospheric forcing predictions from gravity waves in both the middle and upper atmosphere. Further studies will include the time dependence of the tides and extend these studies to 3D.

Acknowledgments
Research by Christopher Heale was carried out under NSF grant AGS-1822551, Katrina Bossert was supported under NSF grant AGS-1822585, and Sharon Vadas was supported by NSF Grant AGS-1822867. We thank the editor and reviewers for their time and effort in improving this manuscript. Simulation data will be made available at https://commons.erau.edu/dm-secondary-gravity-waves-europe/. AIRS data is publicly available at https://airs.jpl.nasa.gov/data/get&urluscore;data and ECMWF reanalysis datasets are available at https://apps.ecmwf.int/datasets/. Access to the ECMWF data was possible through the special project "Deep vertical propagation of internal gravity waves by AD. Part of this research was conducted within the scope of the German research initiative Role of the middle atmosphere in climate (ROMIC) under grant 01LG1206A provided by the Germany ministry for Education and Research. Partial funding was also provided by the German Science foundation (DFG) via the research unit MSGWaves (GW-TP/DO 1020/9-1, PACOG/RA 1400/6-1).

References

Achatz, U. (2007). Gravity-wave breaking: Linear and primary nonlinear dynamics. *Advances in Space Research*, *40*, 719–733.

Alexander, M. J., & Holton, J. R. (1997). A model study of zonal forcing in the equatorial stratosphere by convectively induced gravity waves. *Journal of the Atmospheric Sciences*, *54*, 408–419. https://doi.org/10.1175/1520-0469(1997)054<0408:AMSOZF>2.0.CO;2

Alexander, M. J., & Holton, J. R. (2004). On the spectrum of vertically propagating gravity waves generated by a transient heat source. *Atmospheric Chemistry and Physics*, *4*, 923–932. https://doi.org/10.5194/acp-4-923-2004

Alexander, M. J., & Rosenlof, K. H. (1996). Nonstationary gravity wave forcing of the stratospheric zonal mean wind. *Journal of Geophysical Research*, *101*(D18), 23,465–23,474. https://doi.org/10.1029/96JD02197

Alexander, M. J., & Rosenlof, K. H. (2003). Gravity-wave forcing in the stratosphere: Observational constraints from the Upper Atmosphere Research Satellite and implications for parameterization in global models. *Journal of Geophysical Research*, *108*(D19), 4597. https://doi.org/10.1029/2003JD003373

Andreassen, Ø., Wasberg, C. E., Fritts, D. C., & Isler, J. R. (1994). Gravity wave breaking in two and three dimensions, 1, Model description and comparison of two-dimensional evolutions. *Journal of Geophysical Research*, *99*, 8095–8108.

Aumann, H. H., Chahine, M. T., Gautier, C., Goldberg, M. D., Kalnay, E., McMillin, L. M., et al. (2003). AIRS/AMSU/HSB on the aqua mission: Design, science objectives, data products, and processing systems. *IEEE Transactions on Geoscience and Remote Sensing*, *41*(2), 253–264.

Bacmeister, J. T. (1993). Mountain-wave drag in the stratosphere and mesosphere inferred from observed winds and a simple mountain-wave parameterization scheme. *Journal of the Atmospheric Sciences*, *50*(3), 377–399. https://doi.org/10.1175/1520-0469(1993)050<0377:MWDITS>2.0.CO;2

Bacmeister, J. T., & Schoeberl, M. R. (1989). Breakdown of vertically propagating two-dimensional gravity waves forced by orography. *Journal of the Atmospheric Sciences*, *46*(14), 2109–2134. https://doi.org/10.1175/1520-0469(1989)046<2109:BOVPTD>2.0.CO;2

Baldwin, M. P., Gray, L. J., Dunkerton, T. J., Hamilton, K., Haynes, P. H., Randel, W. J., et al. (2001). The quasi-biennial oscillation. *Reviews of Geophysics*, *39*(2), 179–229. https://doi.org/10.1029/1999RG000073

Bale, D. S., LeVeque, R. J., Mitran, S., & Rossmanith, J. A. (2002). A wave propagation method for conservation laws and balance laws with spatially varying flux functions. *Journal of Scientific Computing*, *24*(3), 955–978.

Becker, E., & Vadas, S. L. (2018). Secondary gravity waves in the winter mesosphere: Results from a high-resolution global circulation model. *Journal of Geophysical Research: Atmospheres*, *123*, 2605–2627. https://doi.org/10.1002/2017JD027460

Beres, J. H. (2004). Gravity wave generation by a three-dimensional thermal forcing. *Journal of the Atmospheric Sciences*, *61*, 1805–1815.

Booker, J. R., & Bretherton, F. P. (1967). The critical layer for internal gravity waves in a shear flow. *Journal of Fluid Mechanics*, *27*, 513–539.

Bossert, K., Fritts, D., Pautet, P. D., Williams, B. P., Taylor, M. J., Kaifler, B., et al. (2015). Momentum flux estimates accompanying multiscale gravity waves over Mount Cook, New Zealand, on 13 July 2014 during the DEEPWAVE campaign. *Journal of Geophysical Research: Atmospheres*, *120*, 9323–9337. https://doi.org/10.1002/2015JD023197

Bossert, K., Kruse, C. G., Heale, C. J., Fritts, D. C., Williams, B. P., Snively, J. B., et al. (2017). Secondary gravity wave generation over New Zealand during the DEEPWAVE campaign. *Journal of Geophysical Research: Atmospheres*, *122*, 7834–7850. https://doi.org/10.1002/2016JD026079

Bramberger, M., Dörnbrack, A., Bossert, K., Ehard, B., Fritts, D. C., Kaifler, B., et al. (2017). Does strong tropospheric forcing cause large-amplitude mesospheric gravity waves? A DEEPWAVE case study. *Journal of Geophysical Research: Atmospheres*, *122*, 11,422–11,443. https://doi.org/10.1002/2017JD027371

Broutman, D., & Young, W. (1986). On the interaction of small-scale oceanic internal waves with near-inertial waves. *Journal of Fluid Mechanics*, *166*, 341–358.

Chun, H. Y., & Kim, Y. H. (2008). Secondary waves generated by breaking of convective gravity waves in the mesosphere and their influence in the wave momentum flux. *Journal of Geophysical Research*, *113*, D23107. https://doi.org/10.1029/2008JD009792

Dörnbrack, A. (1998). Turbulent mixing by breaking gravity waves. *Journal of Fluid Mechanics*, *375*, 113–141. https://doi.org/10.1017/S0022112098002833

Dörnbrack, A., Gisinger, S., Pitts, M. C., Poole, L. R., & Maturilli, M. (2017). Multilevel cloud structures over Svalbard. *Monthly Weather Review*, *145*(4), 1149–1159.

Dörnbrack, A., Leutbecher, M., Kivi, R., & Kyro, E. (1999). Mountain-wave induced record low stratospheric temperatures above northern Scandinavia. *Tellus: Series A*, *51*, 951–963.

Drob, D. P., Emmert, J. T., Crowley, G., Picone, J. M., Shepherd, G. G., Skinner, W., et al. (2008). An empirical model of the Earth's horizontal wind fields: HWM07. *Journal of Geophysical Research*, *113*, A12304. https://doi.org/10.1029/2008JA013668

Dunkerton, T. J. (1997). The role of gravity waves in the quasi-biennial oscillation. *Journal of Geophysical Research*, *102*(D22), 26,053–26,076. https://doi.org/10.1029/96JD02999

Durran, D., & Klemp, J. (1987). Another look at downslope winds. Part II: Nonlinear amplification beneath wave-overturning layers. *Journal of the Atmospheric Sciences*, *44*, 3402–3412.

Eckermann, S. D. (1997). Influence of wave propagation on the Doppler spreading of atmospheric gravity waves. *Journal of Atmospheric Sciences*, *54*, 2554–2573.

Eckermann, S. D., Broutman, D., Ma, J., Doyle, J. D., Pautet, P. D., Taylor, M. J., et al. (2016). Dynamics of orographic gravity waves observed in the mesosphere over the Auckland Islands during the Deep Propagating Gravity Wave Experiment (DEEPWAVE). *Journal of the Atmospheric Sciences*, *73*(10), 3855–3876. https://doi.org/10.1175/JAS-D-16-0059.1

Ehard, B., Achtert, P., Dörnbrack, A., Gisinger, S., Gumbel, J., Khaplanov, M., et al. (2016). Combination of Lidar and model data for studying Deep Gravity Wave Propagation. *Monthly Weather Review*, *144*(1), 77–98. https://doi.org/10.1175/MWR-D-14-00405.1

Ehard, B., Kaifler, B., Dörnbrack, A., Preusse, P., Eckermann, S. D., Bramberger, M., et al. (2017). Horizontal propagation of large-amplitude mountain waves into the polar night jet. *Journal of Geophysical Research: Atmospheres*, *122*, 1423–1436. https://doi.org/10.1002/2016JD025621

Ehard, B., Malardel, S., Dörnbrack, A., Kaifler, B., Kaifler, N., & Wedi, N. (2018). Comparing ECMWF high-resolution analyses with lidar temperature measurements in the middle atmosphere. *Quarterly Journal of the Royal Meteorological Society*, *144*(712), 633–640.

Ern, M., Ploeger, F., Preusse, P., Gille, J. C., Gray, L. J., Kalisch, S., et al. (2014). Interaction of gravity waves with the QBO: A satellite perspective. *Journal of Geophysical Research: Atmospheres*, *119*, 2329–2355. https://doi.org/10.1002/2013JD020731

Franke, P., & Robinson, W. (1999). Nonlinear behavior in the propagation of atmospheric gravity waves. *Journal of the Atmospheric Sciences*, *56*, 3010–3027.

Fritts, D. C., & Alexander, M. J. (2003). Gravity wave dynamics and effects in the middle atmosphere. *Review Geophysics*, *41*(1), 1003. https://doi.org/10.1029/2001RG000106

Fritts, D. C., Smith, R. B., Taylor, M. J., Doyle, J. D., Eckermann, S. D., Drnbrack, A., et al. (2016). The Deep Propagating Gravity Wave Experiment (DEEPWAVE): An airborne and ground-based exploration of gravity wave propagation and effects from their sources throughout the lower and middle atmosphere. *Bulletin of the American Meteorological Society*, *97*, 425–453. https://doi.org/10.1175/BAMS-D-14-00269.1

Fritts, D. C., Vosper, S. B., Williams, B. P., Bossert, K., Plane, J. M. C., Taylor, M. J., et al. (2018). Large-amplitude mountain waves in the mesosphere accompanying weak cross-mountain flow during DEEPWAVE Research Flight RF22. *Journal of Geophysical Research: Atmospheres*, *123*, 9992–10,022. https://doi.org/10.1029/2017JD028250

Fritts, D. C., Wang, L., Werne, J., Lund, T., & Wan, K. (2009). Gravity wave instability and dynamics at high Reynolds numbers. Part I: Wave field evolution at large amplitudes and high frequencies. *Journal of the Atmospheric Sciences*, *66*, 1126–1147.

Garcia, R. R., & Solomon, S. (1985). The effect of breaking gravity waves on the dynamics and chemical composition of the mesosphere and lower thermosphere. *Journal of Geophysical Research*, *90*, 3850–3868.

Heale, C. J., Bossert, K., Snively, J. B., Fritts, D. C., Pautet, P. D., & Taylor, M. J. (2017). Numerical modeling of a multiscale gravity wave event and its airglow signatures over Mount Cook, New Zealand, during the DEEPWAVE campaign. *Journal of Geophysical Research: Atmospheres*, *122*, 846–860. https://doi.org/10.1002/2016JD025700

Heale, C. J., & Snively, J. B. (2015). Gravity wave propagation through a vertically and horizontally inhomogeneous background wind. *Journal of Geophysical Research: Atmospheres*, *120*, 5931–5950. https://doi.org/10.1002/2015JD023505

Heale, C. J., Snively, J. B., Hickey, M. P., & Ali, C. J. (2014). Thermospheric dissipation of upward propagating gravity wave packets. *Journal of Geophysical Research: Atmospheres*, *119*, 3857–3872. https://doi.org/10.1002/2013JA019387

Heale, C. J., Walterscheid, R. L., & Snively, J. B. (2018). Localization effects on the dissipation of gravity wave packets in the upper mesosphere and lower thermosphere. *Journal of Geophysical Research: Atmospheres*, *123*, 8915–8935. https://doi.org/10.1029/2017JD027617

Hickey, M. P., Walterscheid, R. L., & Schubert, G. (2011). Gravity wave heating and cooling of the thermosphere: Roles of the sensible heat flux and viscous flux of kinetic energy. *Journal of Geophysical Research*, *116*, A12326. https://doi.org/10.1029/2010JA016792

Hoffmann, L., & Alexander, M. J. (2009). Retrieval of stratospheric temperatures from Atmospheric Infrared Sounder radiance measurements for gravity wave studies. *Journal of Geophysical Research*, *114*, D07105. https://doi.org/10.1029/2008JD011241

Hoffmann, L., Xue, X., & Alexander, M. J. (2013). A global view of stratospheric gravity wave hotspots located with Atmospheric Infrared Sounder observations. *Journal of Geophysical Research: Atmospheres*, *118*, 416–434. https://doi.org/10.1029/2012JD018658

Hólm, E., Forbes, R., Lang, S., Magnusson, L., & Malardel, S. (2016). New model cycle brings higher resolution. *ECMWF Newsletter*, *147*, 14–19. http://www.ecmwf.int/sites/default/files/elibrary/2016/16299-newsletter-no147-spring-2016.pdf

Holton, J. R. (1982). The role of gravity wave induced drag and diffusion in the momentum budget of the mesosphere. *Journal of the Atmospheric Sciences*, *39*, 791–799.

Holton, J. R. (1983). The influence of gravity wave breaking on the general circulation of the middle atmosphere. *Journal of the Atmospheric Sciences*, *40*, 2497–2507.

Holton, J. R., & Alexander, M. J. (2000). The role of waves in the transport circulation of the middle atmosphere. In G. M. Ser (Ed.), *Atmospheric Science Across the Stratopause* (Vol. 123, pp. 21–35).

Horinouchi, T., Nakamura, T., & Kosaka, J. i. (2002). Convectively generated mesoscale gravity waves simulated throughout the middle atmosphere. *Geophysical Research Letters*, *29*(21), 2007. https://doi.org/10.1029/2002GL016069

Jacobi, C. (2012). 6 year mean prevailing winds and tides measured by VHF meteor radar over Collm (51.3N, 13.0E). *Journal of Atmospheric and Solar-Terrestrial Physics*, *78–79*, 8–18.

Kaifler, B., Kaifler, N., Ehard, B., Dörnbrack, A., Rapp, M., & Fritts, D. C. (2015). Influences of source conditions on mountain wave penetration into the stratosphere and mesosphere. *Geophysical Research Letters*, *42*, 9488–9494. https://doi.org/10.1002/2015GL066465

Kaifler, N., Kaifler, B., Ehard, B., Gisinger, S., Dörnbrack, A., Rapp, M., & Liley, B. (2017). Observational indications of downward-propagating gravity waves in middle atmosphere lidar data. *Journal of Atmospheric and Solar-Terrestrial Physics*, *162*, 16–27. https://doi.org/10.1016/j.jastp.2017.03.003

Kim, Y. H., & Chun, H. Y. (2008). Effects of the basic-state wind on secondary waves generated by the breaking of gravity waves in the mesosphere. *Asia-Pacific Journal of Atmospheric Sciences*, *45*(1), 91–100.

Kim, Y. J., Eckermann, S. D., & Chun, H. Y. (2003). A overview of the past, present, and future of gravity wave drag parameterization for numerical climate and weather prediction models. *Atmosphere-Ocean*, *41*, 65–98.

Lane, T. P., Reeder, M. J., & Clark, T. L. (2001). Numerical modeling of gravity wave generation by deep tropical convection. *Journal of the Atmospheric Sciences*, *58*, 1249–1274.

LeVeque, R. J. (2002). *Finite Volume Methods for Hyperbolic Problems*. Cambridge: Cambridge University Press.

LeVeque, R. J., & Berger, M. J. (2004). Clawpack software version 4.6. www.clawpack.org

Lindzen, R. S. (1981). Turbulence and stress owing gravity wave and tidal breakdown. *Journal of Geophysical Research*, *C10*, 9707–9714.

Lund, T. S., & Fritts, D. C. (2012). Numerical simulation of gravity wave breaking in the lower thermosphere. *Journal of Geophysical Research*, *117*, D21105. https://doi.org/10.1029/2012JD017536

Malardel, S., & Wedi, N. P. (2016). How does subgrid-scale parametrization influence nonlinear spectral energy fluxes in global NWP models? *Journal of Geophysical Research: Atmospheres*, *121*, 5395–5410. https://doi.org/10.1002/2015JD023970

McFarlane, N. A. (1987). The effect of orographically excited gravity wave drag on the general circulation of the lower stratosphere and troposphere. *Journal of the Atmospheric Sciences*, *44*, 1775–1800.

McLandress, C., Shepherd, T. G., Polavarapu, S., & Beagley, S. R. (2012). Is missing orographic gravity wave drag near 60°S the cause of the stratospheric zonal wind biases in chemistry—Climate models? *Journal of the Atmospheric Sciences*, *69*(3), 802–818. https://doi.org/10.1175/JAS-D-11-0159.1

Nappo, C. J. (2002). An introduction to atmospheric gravity waves.

Nastrom, G. D., & Fritts, D. (1992). Sources of mesoscale variability of gravity waves, Part I, Topographic excitation. *Journal of the Atmospheric Sciences*, *49*, 101–110.

Piani, C., Durran, D., Alexander, M. J., & Holton, J. R. (2000). A numerical study of three-dimensional gravity waves triggered by deep tropical convection and their role in the dynamics of the QBO. *Journal of the Atmospheric Sciences*, *57*, 3689–3702.

Picone, J. M., Hedin, A. E., Drob, D. P., & Aikin, A. (2002). NRL-MSISE-00 empirical model of the atmosphere: Statisical comparisons and scientific issues. *Journal of Geophysical Research*, *107*(A12), 1468. https://doi.org/10.1029/2002JA009430

Satomura, T., & Sato, K. (1999). Secondary generation of gravity waves associated with the breaking of mountain waves. *Journal of the Atmospheric Sciences*, *56*(22), 3847–3858. https://doi.org/10.1175/1520-0469(1999)056<3847:SGOGWA>2.0.CO;2

Senf, F., & Achatz, U. (2011). On the impact of middle-atmosphere thermal tides on the propagation and dissipation of gravity waves. *Journal of Geophysical Research*, *116*, D24110. https://doi.org/10.1029/2011JD015794

Smith, R. B. (1979). The influence of mountains on the atmosphere. *Advances in Geophysics*, *21*, 87–239.

Smith, R. B., Nugent, A. D., Kruse, C. G., Fritts, D. C., Doyle, J. D., Eckermann, S. D., et al. (2016). Stratospheric gravity wave fluxes and scales during DEEPWAVE. *Journal of the Atmospheric Sciences*, *73*(7), 2851–2869. https://doi.org/10.1175/JAS-D-15-0324.1

Smith, S. M., Vadas, S. L., Baggaley, W. J., Hernandez, G., & Baumgardner, J. (2013). Gravity wave coupling between the mesosphere and thermosphere over New Zealand. *Journal of Geophysical Research: Space Physics*, *118*, 2694–2707. https://doi.org/10.1002/jgra.50263

Snively, J. B. (2013). Mesospheric hydroxyl airglow signatures of acoustic and gravity waves generated by transient tropospheric forcing. *Geophysical Research Letters*, *40*, 1–5. https://doi.org/10.1002/grl.50886

Snively, J., & Pasko, V. P. (2003). Breaking of thunderstorm-generated gravity waves as a source of short-period ducted waves at mesopause altitudes. *Geophysical Research Letters*, *30*(24), 2254. https://doi.org/10.1029/2003GL018436

Snively, J. B., & Pasko, V. P. (2008). Excitation of ducted gravity waves in the lower thermosphere by tropospheric sources. *Journal of Geophysical Research*, *113*, A06303. https://doi.org/10.1029/2007JA012693

Song, I., Chun, H. Y., & Lane, T. P. (2003). Generation mechanisms of convectively forced internal gravity waves and their propagation to the stratosphere. *Journal of the Atmospheric Sciences*, *60*, 1960–1980.

Stephan, C., Alexander, M. J., & Richter, J. H. (2016). Characteristics of gravity waves from convection and implications for their parameterization in global circulation models. *Journal of the Atmospheric Sciences*, *73*, 2729–2742.

Stober, G., Chau, J. L., Vierinen, J., Jacobi, C., & Wilhelm, S. (2018). Retrieving horizontally resolved wind fields using multi-static meteor radar observations. *Atmospheric Measurement Techniques*, *11*, 4891–4907.

Stober, G., Matthias, V., Jacobi, C., Wilhelm, S., Höffner, J., & Chau, J. L. (2017). Exceptionally strong summer-like zonal wind reversal in the upper mesosphere during winter 2015/16. *Annales Geophysicae*, *35*(3), 711–720. https://doi.org/10.5194/angeo-35-711-2017

Torrence, C., & Compo, G. P. (1998). A practical guide to wavelet analysis. *Bulletin of the American Meteorological Society*, *79*(1), 61–q78.

Vadas, S. L. (2007). Horizontal and vertical propagation and dissipation of gravity waves in the thermosphere from lower atmospheric and thermospheric sources. *Journal of Geophysical Research*, *112*, A06305. https://doi.org/10.1029/2006JA011845

Vadas, S. L., & Becker, E. (2019). Numerical modeling of the generation of tertiary gravity waves in the mesosphere and thermosphere during strong mountain wave events over the Southern Andes. *Journal of Geophysical Research: Space Physics*, *124*, 7687–7718. https://doi.org/10.1029/2019JA026694

Vadas, S. L., & Crowley, G. (2010). Sources of the traveling ionospheric disturbances observed by the ionospheric TIDDBIT sounder near Wallops Island on 30 October 2007. *Journal of Geophysical Research*, *115*, A07324. https://doi.org/10.1029/2009JA015053

Vadas, S. L., & Fritts, D. C. (2005). Thermospheric responses to gravity waves: Influences of increasing viscosity and thermal diffusivity. *Journal of Geophysical Research*, *110*, D15103. https://doi.org/10.1029/2004JD005574

Vadas, S. L., Fritts, D. C., & Alexander, M. J. (2003). Mechanism for the generation of secondary waves in wave breaking regions. *Journal of the Atmospheric Sciences*, *60*, 194–214.

Vadas, S. L., Liu, H. L., & Lieberman, R. S. (2014). Numerical modeling of the global changes to the thermosphere and ionosphere from the dissipation of gravity waves from deep convection. *Journal of Geophysical Research: Space Physics*, *119*, 7762–7793. https://doi.org/10.1002/2014JA020280

Vadas, S. L., Xu, S., Yue, J., Bossert, K., Becker, E., & Baumgarten, G. (2019). Characteristics of the quiet-time hot spot gravity waves observed by GOCE over the Southern Andes on 5 July 2010. *Journal of Geophysical Research: Space Physics*, *124*, 7034–7061. https://doi.org/10.1029/2019JA026693

Vadas, S. L., Zhao, J., Chu, X., & Becker, E. (2018). The excitation of secondary gravity waves from body forces: Theory and observation. *Journal of Geophysical Research: Atmospheres*, *123*, 9296–9325. https://doi.org/10.1029/2017JD027970

Yiğit, E., & Medvedev, A. S. (2015). Internal wave coupling processes in Earth's atmosphere. *Advances in Space Research*, *55*, 983–1003. https://doi.org/10.1016/j.asr.2014.11.020.

Zettergren, M. D., & Snively, J. B. (2015). Ionospheric response to infrasonic-acoustic waves generated by natural hazard events. *Journal of Geophysical Research: Space Physics*, *120*, 8002–8024. https://doi.org/10.1002/2015JA021116

Zhou, X., Holton, J. R., & Mullendore, G. L. (2002). Forcing of secondary waves by breaking of gravity waves in the mesosphere. *Journal of Geophysical Research*, *107*(D7), 4058. https://doi.org/10.1029/2001JD001204